communications chemistry

A Nature Portfolio journal

Article

https://doi.org/10.1038/s42004-025-01852-0

Modelling electric field control in a 4f molecular qudit with hyperfine coupling

William T. Morrillo[1], Andrea Mattioni[1], William J. A. Blackmore[1], David P. Mills[1] & Nicholas F. Chilton[1,2]

Understanding the fundamental principles of spin-electric coupling in molecules with hyperfine-coupled electronic and nuclear spins offers a route to electric field-based molecular quantum information. We recently addressed the electronic degrees of freedom in $[Tm\{N(Si^iPr_3)_2\}_2]$. Here, we treat both electronic and $I = 1/2$ nuclear spins explicitly to investigate the possibility of electric field control of the nuclear degrees of freedom. Furthermore, since the hyperfine coupling breaks Kramers degeneracy and therefore spin-electric coupling arises at zeroth-order, we investigate if this the inclusion of the nuclear spin strongly influences the overall coupling. Transitions are classified as EPR-, NMR-, or mixed/forbidden character, revealing that EPR-like transitions couple more strongly to electric fields than NMR-like ones, as crystal-field modulation dominates over hyperfine modulation. The anisotropy of the electric field effect agrees with previous results, but magnetic-field orientation dependence is suppressed by zeroth-order spin-electric coupling. Dissipative spin-dynamics simulations show that experimentally feasible electric field strengths and relaxation times permit coherent manipulation of both the electronic and nuclear spins, demonstrating an experimentally viable pathway for electric field control in $[Tm\{N(Si^iPr_3)_2\}_2]$.

Molecule-based quantum information processing is an emerging research field motivated by the allure of tunable molecular qubits through the chemical design of their ligand field and the selection of metal ions[1]. The presence of multiple unpaired electronic or nuclear spins in molecular complexes enables the realization of *d*-level quantum systems, also known as qudits, going beyond that standard two-level qubit paradigm[2–7]. This aspect of molecular quantum information processing offers significant design advantages over current commercial qubits, potentially reducing the footprint of quantum chips and mitigating fidelity losses in two-qubit gates[8]. The *d*-level system can function as multiple maximally entangled qubits, facilitating the implementation of multi-qubit gates[8].

Molecular qudits are typically realised as spin multiplets, arising either from unpaired electrons, nuclear spins, or a combination of the two via hyperfine coupling (HFC)[2–4,9–13]. The shielded nature of the nucleus results in a significantly longer decoherence time (T_2) compared to electronic degrees of freedom, allowing quantum states to be manipulated and stored up to several microseconds[2,14]. For this reason, hyperfine-coupled electronic and nuclear spin degrees of freedom in molecules have been proposed as building blocks for quantum technologies[15], with applications ranging from quantum simulation[6,16], to quantum sensing[8] and fault-tolerant quantum computing[17–19]. Furthermore, the DiVincenzo criteria necessitate a quantum architecture to possess a complete set of quantum gates, some of which require more than two degrees of freedom for their implementation, such as the controlled-NOT (CNOT) gate[20]. Most quantum architectures necessitate the utilisation of multiple entangled qubits to implement these quantum gates, which frequently serves as a source of decoherence[21]. However, molecular qudits offer a promising resolution regarding their tunable Hilbert space. Consequently, some of us have investigated the application of inverse design to identify candidate molecular qudits capable of executing quantum algorithms within a single molecule[7]. The primary challenge lies in the ability to spectrally address each transition within the molecular qudit without spectral crowding while maintaining adherence to the resonator's bandwidth; in the case of a four-level system, the rhombicity of the zero-field splitting spin Hamiltonian should be maximised.

In order for a qubit to be useful, it should be possible to individually address and coherently manipulate it without affecting its neighbours. This challenge cannot be overcome by standard techniques for molecular spin manipulation, which are dominated by pulsed electron paramagnetic resonance (EPR) and nuclear magnetic resonance (NMR) spectroscopies, since these techniques employ oscillating magnetic fields to achieve coherent driving and magnetic fields are not easily confined to the nanoscale. Electric field control of molecular qubits and qudits presents a potential solution to this

[1]Department of Chemistry, The University of Manchester, Manchester, UK. [2]Research School of Chemistry, The Australian National University, Canberra, Australia. e-mail: nicholas.chilton@anu.edu.au

limitation owing to the ability to precisely and selectively apply electric fields at the atomic scale, epitomised by scanning tunnelling microscopy. The microscopic basis for this control strategy leverages the spin-electric coupling (SEC), which is responsible for coupling electric and magnetic properties in materials[22]. Molecular SEC effects have been observed in $[Fe_3O(PhCOO)_6(Py)_3]ClO_4$.py, attributed to the strong Dzyaloshinskii–Moriya antisymmetric exchange in the Fe_3 system[23]. An elegant demonstration of SEC was also performed at clock transitions in $[Ho(W_5O_18)_2]^{9-}$, where the applied electric field caused a lowering of symmetry, giving rise to an additional phase at the clock transition which sustained quantum coherence on a microsecond timescale[24,25]. Most recently, SEC was observed in monometallic [Mn(me_6tren)X]Y_2 (X and Y can be either Cl and ClO_4, Br and PF_6, or I and I, respectively)[26]. Despite the absence of strong spin-orbit coupling in Mn, the high C_3 symmetry coupled to the magnetic anisotropy of the system leads to substantial SEC whose magnitude is comparable to previously measured lanthanide molecules with large spin-orbit coupling[25,27]. Stronger SEC was observed for X = I, which was attributed to its greater polarizability compared to Br or Cl; these results echo our recent computational findings[28].

While SEC relies on spin-orbit coupling[29], its origin can arise from many different physical processes, but in the case of lanthanide molecules which have strong spin-orbit coupling, we have focussed on electric field-induced molecular distortions that perturb the effective crystal field potential[28]. However, in the case of half-integer spin systems, electric fields cannot generate SEC on their own. This is due to the Kramers time-reversal invariance theorem, which means that time-even operators (such as electric fields, or changes in the crystal field potential) cannot have off-diagonal matrix elements between the twofold degenerate electronic states. Therefore, in order to observe SEC in this context, a magnetic field that breaks the time-reversal symmetry must be introduced. This scenario was considered in our previous work[28], where we observed a pronounced dependence of SEC on the orientation of electric and magnetic fields, leading to the conclusion that SEC is predominantly generated by electric field-induced molecular distortions that break spatial symmetry.

In this work, we investigate the effects of the inclusion of the hyperfine-coupled nuclear spin degrees of freedom on the SEC. Given that HFC to the nuclear spin breaks the Kramers degeneracy, SEC may be achieved in molecular qudits in zero magnetic field. As such, we investigate the modulation of the HFC due to an applied electric field, showing that this can drive transitions within the nuclear degrees of freedom. We determine the magnetic and electric field orientation dependence of the SEC and show that HFC can boost SEC by several orders of magnitude for specific field orientations, and elucidate the symmetry dependence of the modulation of the HFC. Furthermore, we show that SEC can be used to selectively drive transitions between hyperfine states under realistic conditions, by simulating the dissipative spin dynamics of the low-energy multiplet under a coherent electric field.

Methods

Computational details

The equilibrium and electric field distorted molecular geometries were taken from our previous work where the computational methods for these optimizations are detailed[28]. Complete active space self-consistent spin-orbit calculations (CASSCF-SO) were performed in OpenMolcas v23.06 (adapted to print the X2C decoupling matrices) for both the equilibrium molecular geometry and the molecular geometries distorted by an applied electric field. We used a minimal active space with 13 electrons in 7 orbitals to model the $4f^{13}$ electron configuration of Tm^{2+}[30–32]. The electronic structure was computed at the CASSCF level of theory including scalar relativistic effects using the exact two-component (SR-X2C) decomposition and spin-orbit coupling using the AMFI approximation[33–36]. Tm was equipped with the ANO-RCC-VTZP basis set, while all other atoms were equipped with ANO-RCC-VDZP basis sets. The resolution of identity approximation was used to treat the two-electron integrals with the acCD auxiliary basis set[37]. The X2C decoupling matrices were used to compute the HFC tensor using Hyperion[38]. The crystal field parameters were obtained through the projection of the ab initio Hamiltonian onto a model crystal field Hamiltonian using `angmom_suite`[39].

Model Hamiltonian construction

The crystal field Hamiltonian $\hat{\boldsymbol{H}}_{\mathrm{CF}}$ is constructed as a linear combination of Stevens operators $\hat{\boldsymbol{O}}_k^q$ of rank k and order q constructed in the total angular momentum basis, weighted by crystal field parameters B_k^q and operator equivalent factors θ_k for even $k = 2, 4, 6$ terms of the $^2F_{7/2}$ manifold.

$$\hat{\boldsymbol{H}}_{\mathrm{CF}}^{J} = \sum_{k=0}^{k_{\max}} \sum_{q=-k}^{+k} \theta_k B_k^q \hat{\boldsymbol{O}}_k^q \tag{1}$$

The superscript J denotes the total electronic angular momentum basis. The electronic Zeeman Hamiltonian $\hat{\boldsymbol{H}}_{\mathrm{EZ}}$ is constructed from the total angular momentum operator of the $^2F_{7/2}$ manifold as

$$\hat{\boldsymbol{H}}_{\mathrm{EZ}}^{J} = \mu_B g_J \boldsymbol{B} \cdot \hat{\boldsymbol{J}} \tag{2}$$

where μ_B and g_J denote the Bohr magneton and Landé g-factor, respectively. We couple the electronic and nuclear degrees of freedom with the hyperfine interaction Hamiltonian $\hat{\boldsymbol{H}}_{\mathrm{HF}}$ which is constructed from the total angular momentum operator of the electronic degrees of freedom, the nuclear spin operators $\hat{\boldsymbol{I}}$, and the HFC tensor A.

$$\hat{\boldsymbol{H}}_{\mathrm{HF}}^{JI} = \sum_i \sum_k A_{ik} \hat{\boldsymbol{J}}_i \otimes \hat{\boldsymbol{I}}_k \tag{3}$$

The Hyperfine interaction Hamiltonian is defined in the uncoupled basis denoted by the superscript JI. The nuclear Zeeman Hamiltonian $\hat{\boldsymbol{H}}_{\mathrm{NZ}}$ for the $I = 1/2$ nuclear spin of ^{169}Tm is given by

$$\hat{\boldsymbol{H}}_{\mathrm{NZ}}^{I} = -\mu_n g_n \boldsymbol{B} \cdot \hat{\boldsymbol{I}} \tag{4}$$

where μ_n is the nuclear magneton and $g_n = -0.462$ is the nuclear g-factor[40]. We subsequently diagonalize the total Hamiltonian via the unitary transformation $\hat{\boldsymbol{U}}_{\mathrm{eq}}$

$$\hat{\boldsymbol{H}}_{\mathrm{eq}} = \hat{\boldsymbol{U}}_{\mathrm{eq}}^{\dagger} \left(\hat{\boldsymbol{H}}_{\mathrm{CF}}^{J} \otimes \mathbb{1}^{I} + \hat{\boldsymbol{H}}_{\mathrm{EZ}}^{J} \otimes \mathbb{1}^{I} + \hat{\boldsymbol{H}}_{\mathrm{HF}}^{JI} + \mathbb{1}^{J} \otimes \hat{\boldsymbol{H}}_{\mathrm{NZ}}^{I} \right) \hat{\boldsymbol{U}}_{\mathrm{eq}} \tag{5}$$

where the subscript "eq" indicates that this Hamiltonian corresponds to the equilibrium molecular geometry, and $\mathbb{1}$ indicates the identity matrix of the appropriate dimension for the J or I space in the superscript. With the same method, we determine the crystal field and hyperfine Hamiltonians for a molecular structure distorted by an electric field, yielding a spin Hamiltonian $\hat{H}_{\mathrm{dist}}$ completely analogous to (5), which we rotate onto the equilibrium eigenbasis through $\hat{\boldsymbol{U}}_{\mathrm{eq}}$, i.e. $\hat{\boldsymbol{H}}_{\mathrm{dist}} = \hat{\boldsymbol{U}}_{\mathrm{eq}}^{\dagger} \hat{\boldsymbol{H}}_{\mathrm{dist}}^{JI} \hat{\boldsymbol{U}}_{\mathrm{eq}}$. The SEC Hamiltonian is then represented by the difference between the equilibrium and the distorted Hamiltonian in the eigenbasis at equilibrium (note that the dropping of the JI basis notation signals that operators have been rotated into the eigenstate basis of $\hat{\boldsymbol{H}}_{\mathrm{eq}}$).

$$\hat{\boldsymbol{H}}_{\vec{E}} = \hat{\boldsymbol{H}}_{\mathrm{dist}} - \hat{\boldsymbol{H}}_{\mathrm{eq}} \tag{6}$$

We note that the hyperfine-coupled eigensystem is not time-reversal symmetric and so the ground quartet manifold comprised of the electronic ground Kramers doublet and the nuclear spin ($S_{\mathrm{eff}} \otimes I = 1/2 \otimes 1/2$) is non-degenerate. The electric field Hamiltonian $\hat{\boldsymbol{H}}_{\vec{E}}$ contains diagonal matrix elements that correspond to energy shifts due to the applied electric field, and crucially non-zero off diagonal matrix elements that correspond to SEC between states. We define the SEC between two states $|\psi_i\rangle$ and $|\psi_j\rangle$ by the magnitude of the off-diagonal matrix element in the electric field Hamiltonian that mixes them $|\langle\psi_i|\hat{\boldsymbol{H}}_{\vec{E}}|\psi_j\rangle|$.

To calculate the derivative of the HFC A with respect to nuclear displacements, we use a finite difference approach. We employ the analytic linear electric field approximation model[28] to obtain finite differences in molecular structure with respect to a small change in electric field for each

Cartesian orientation of the electric field. We then perform CAS[13,7]SCF calculations on these structures followed by calculation of the HFC with Hyperion to obtain the HFC tensor. Thus, we can access derivatives of the HFC Hamiltonian with respect to the electric field, $\nabla_{\boldsymbol{E}}\hat{\boldsymbol{H}}_{\mathrm{HF}}$; we defer further details to the SI.

EPR

Crystalline $[Tm\{N(Si^iPr_3)_2\}_2]$ was prepared according to published procedures[41]. Crystals were ground using a mortar and pestle to obtain a microcrystalline powder before being transferred to an X-band EPR tube and flame-sealed under vacuum. Continuous wave (CW) EPR spectra of polycrystalline $[Tm\{N(Si^iPr_3)_2\}_2]$ were obtained at X-band (9.39113 GHz) using a Bruker EMXPlus spectrometer equipped with a Bruker 4122-SHQ resonator. A temperature of 5.3 K was achieved using a ColdEdge Stinger closed-cycle He cryocooler mated to an Oxford Instruments ESR900 cryostat. Temperature measurement and control was handled via an Oxford Instruments MercuryITC. We simulated the EPR spectra using ab initio calculated crystal field parameters B_k^q and HFC constants in PHI (v3.1.6)[42]. The simulation used powder integration and empirical anisotropic Lorentzian line widths of 0.5, 0.4, and 0.03 GHz aligned to g_x, g_z, and g_y, respectively.

Results and discussion

EPR

CW X-band EPR data of polycrystalline $[Tm\{N(Si^iPr_3)_2\}_2]$ shows a typical spectra for a rhombic spin $S_{\mathrm{eff}} = 1/2$ ion with each g-feature split by HFC with the $I = 1/2$ nucleus (Fig. 1). Hyperfine split transitions corresponding to g_1, g_2 and g_3 are centred at ~110, 210 and 610 mT. The data is in excellent agreement with the previously published EPR data,[41] though in this work we have resolution of the hyperfine splitting of the high-field transition. The data can be fitted using Easy-Spin[40] to a model Hamiltonian where we treat the ground electronic Kramers doublet as an effective spin $S_{\mathrm{eff}} = 1/2$ and extract the effective HFC tensor A_{eff} and effective g-matrix g_{eff}:

$$\hat{\boldsymbol{H}}_{\mathrm{fit}} = \hat{\boldsymbol{S}}_{\mathrm{eff}} \cdot A_{\mathrm{eff}} \cdot \hat{\boldsymbol{I}} - \mu_n g_n \boldsymbol{B} \cdot \hat{\boldsymbol{I}} + \mu_B \boldsymbol{B} \cdot g_{\mathrm{eff}} \cdot \hat{\boldsymbol{S}}_{\mathrm{eff}} \tag{7}$$

Here we assume that A_{eff} and g_{eff} are collinear, which gives best-fit parameters $g_1 = 1.084(2)$, $g_2 = 3.027(2)$, $g_3 = 5.7(5)$, $|A_1| = 300(220)$MHz, $|A_2| = 1072(760)$MHz and $|A_3| = 1905(115)$MHz, where parentheses on the g-factors indicate the g-strain, and on the HFCs they indicate the anisotropic line broadening. The extracted parameters are in excellent agreement with the previous data[41].

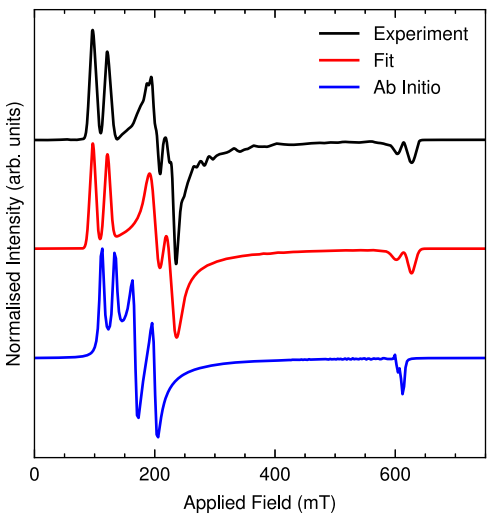

Fig. 1 | Experimental EPR spectrum. CW X-band EPR data of polycrystalline $[Tm\{N(Si^iPr_3)_2\}_2]$ performed at 5.3 K (black). The data was fitted to Eq. (7) in Easy-Spin[40] (red) with good agreement between experiment and model (see text). The simulated CW X-band EPR spectra calculated using the ab initio crystal field parameters and hyperfine coupling constant (blue).

Our CASSCF-SO calculations give $g_1 = 1.15$, $g_2 = 3.67$, $g_3 = 5.44$, and the HFC tensor calculated using Hyperion[38] gives eigenvalues for the equilibrium geometry of 357.57, −1222.05, and −1823.58 MHz for A_1, A_2, and A_3, respectively. These are in remarkable agreement with the experimental values, which gives us confidence to assign the signs of the experimental parameters as matching the CASSCF ones.

Spin-electric coupling of hyperfine coupled states

Previously, we have elucidated that the SEC originates from symmetry-breaking molecular distortions induced by an applied external electric field and is highly sensitive to magnetic field orientation as a consequence of magnetic anisotropy[28]. However, the validity of these criteria remains unproven for systems that exhibit HFC. As mentioned above, a fundamental distinction when considering a system with coupled electronic and nuclear spins is that the degeneracy of the Kramers states can be broken by HFC in the absence of a magnetic field. This is evident in Zeeman plots of the lowest four eigenstates of the equilibrium Hamiltonian (5), which we denote as $|\psi_i\rangle$ with $i = 1, \ldots, 4$ (Fig. 2a). Here, and subsequently, we define the Cartesian axes such that x, y, z align with g_1, g_3, g_2, respectively. Intriguingly, there is an avoided crossing at zero magnetic field between states $|\psi_2\rangle$ and $|\psi_3\rangle$ with a field along x or z, but this switches to two avoided crossings between $|\psi_1\rangle$ and $|\psi_2\rangle$ and $|\psi_3\rangle$ and $|\psi_4\rangle$ when the field is along y. This occurs because $|\psi_2\rangle$ ($|\psi_3\rangle$) has a positive (negative) curvature along x and z, but a negative (positive) curvature along y. Hence, there must exist an intermediate field orientation where $|\psi_2\rangle$ and $|\psi_3\rangle$ switch from positive to negative curvature, which results in a special turning point where the derivative of the eigenstate energies as a function of field is zero to higher orders; for this molecule the orientations are $\boldsymbol{e}_A = (0, 0.377, 0.926)$ and $\boldsymbol{e}_B = (0.977, 0.211, 0)$. This should, in principle, greatly enhance the effective clock protection of the associated transitions (Figs. S12, S13, and S14)[24]. Interestingly, enhancing the effective clock protection of these transitions gives rise to enhanced SEC at small magnetic fields around the avoided crossing (Figs. S30–S35).

As previously mentioned, the inclusion of the HFC between the electronic and nuclear degrees of freedom results in a non-degenerate ground quartet. Consequently, the magnetic field magnitude dependence of the SEC will be intricate. We can investigate this behaviour by plotting the SEC as a heat map in which both the electric field and magnetic field are varied in magnitude and orientation (Figs. S24–S29). When both the magnetic and electric fields are oriented along y, we observe sharp turning-points in the SEC at the crossing of states $|\psi_2\rangle$ and $|\psi_3\rangle$ (Fig. S27). Here, the SEC decreases by approximately a factor of two, but we do not elaborate further on this phenomena as we aim to maximise the coupling to the electric field.

To elucidate the magnetic and electric field orientation dependence of the SEC, we analyse the SEC between all pairs of states within the ground quartet as a function of electric field strength for all Cartesian orientations of $\boldsymbol{E}$ and $\boldsymbol{B}$. We start with a fixed magnetic field strength of 320 mT for consistency with our previous work[28]. The results are shown in Fig. 3, where transitions within the ground quartet are colour-coded according to the dominant character of the transition between them: electronic/EPR-like (red), nuclear/NMR-like (blue) and mixed (green; forbidden EPR/NMR transitions). This classification corresponds to Fig. 2c and assigning the dominant contribution to the eigenfunctions which become clearer in larger magnetic fields (see Supplementary Note 2 for further details).

In most cases, we observe a significant magnetic and electric field dependence of the SEC, with some of the couplings increasing up to two orders of magnitude in the E_y, B_y case compared to our previous work[28]. While the inclusion of HFC results in more complex SEC trends, the behaviour of the EPR-like transitions remain similar to the ones we previously determined in the absence of nuclear spin (Fig. S18)[28].

We observe that the SEC is generally stronger for EPR-like transitions than for NMR-like transitions. This is expected since perturbations of the crystal field affect electronic degrees of freedom much more directly than nuclear spins. We can verify this rationale by comparing the derivatives of the

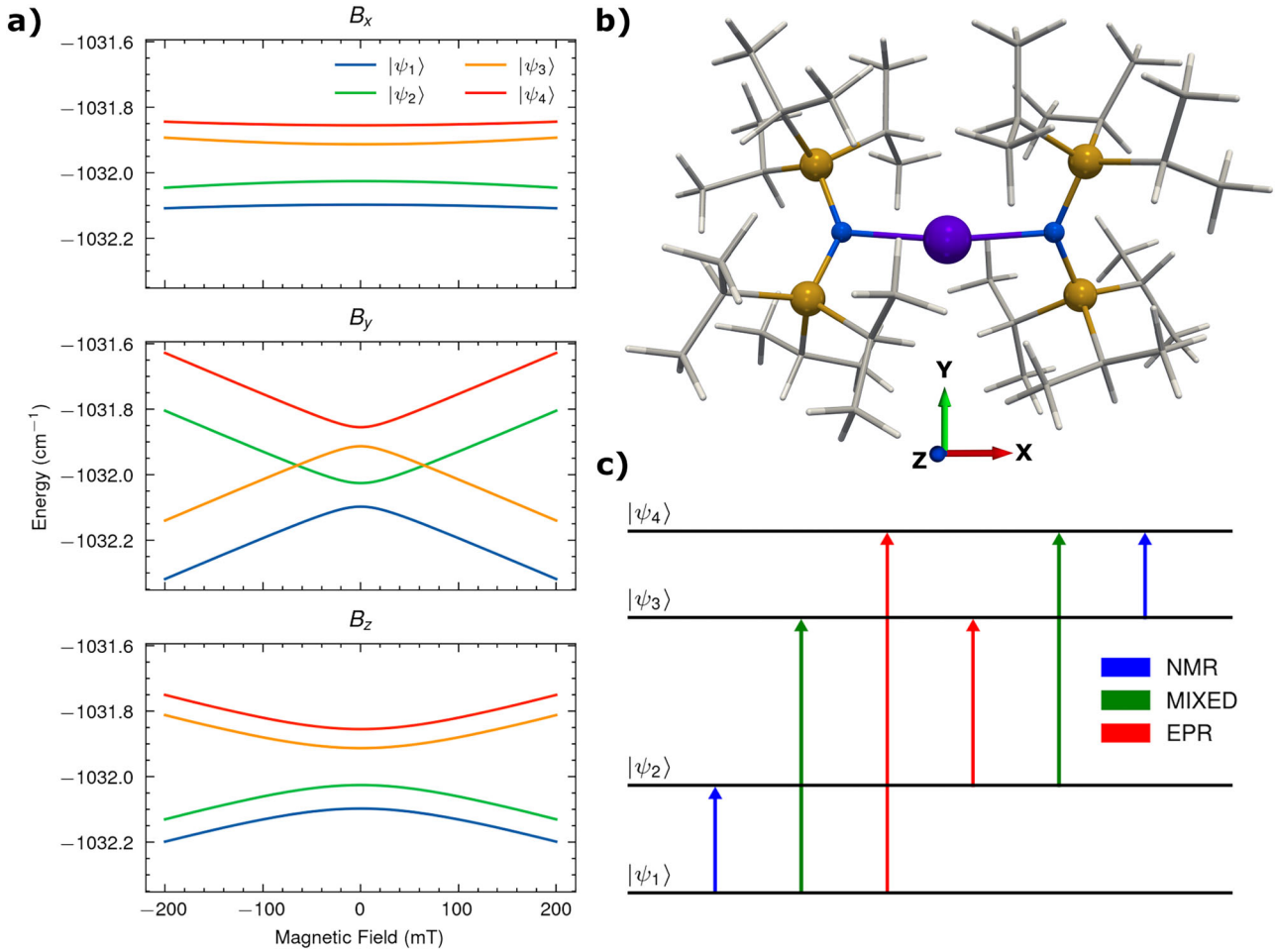

Fig. 2 | Anisotropy and transition character. a Energy of the ground quartet of states as a function of magnetic field strength for three different field orientations. The energy is determined by the eigenvalues of $\hat{H}_{eq}$(5). **b** The gas phase optimised structure of [Tm{N(Si^{i}Pr$_3$)$_2$}$_2$]. Carbon and hydrogen atoms have been omitted (Tm: purple; N: blue; Si: yellow, C: grey sticks; H, white sticks). **c** An energy level diagram (not to scale) showing the assigned EPR-like (red), NMR-like (blue), and mixed-character (green) transitions within the ground quartet.

crystal field and HFC Hamiltonians with respect to the electric field, finding that the latter are a factor 10^7 smaller than the former Supplementary Note 6. Interestingly, the magnitude of SEC for the mixed/forbidden transitions does not always fall in between electronic and nuclear ones (Fig. 3). In some cases, e.g. E_y, B_y, it represents the largest SEC contribution within the ground quartet, suggesting that these classically-forbidden transitions may effectively be probed using electric field drives; we will discuss this in more detail below.

Focussing on the dependence of SEC on the orientation of the electric field, we generally observe smaller couplings when the electric field is oriented along y. As discussed in our original work,[28] this is because the y-axis is coincident with an approximate C_2 symmetry axis passing through the Tm centre, and so the electric field-induced distortions preserve the symmetry leading to smaller off-diagonal crystal field elements than when distortions break the symmetry. Additionally, we observe similar trends when we calculate the SEC for smaller, more experimentally-feasible electric fields (Supplementary Fig. S19).

We now explore the SEC in the absence of a magnetic field, finding that the correlation between symmetry breaking distortions and SEC magnitude becomes even more evident (Figs. S2 and S4). Although all transitions at $|\boldsymbol{B}| = 0$ have mixed character, the SECs for some transitions are two orders of magnitude smaller when the electric field is oriented along the high-symmetry axis (E_y) compared to when symmetry is broken (E_x and E_z).

We can gain further insights into the trends shown in Fig. 3 by considering how the states in the ground quartet are perturbed by the Zeeman terms in Eq. (5), which we collectively denote as $\hat{\boldsymbol{H}}_{Zee}$. Denoting the zero-field ($|\boldsymbol{B}| = 0$) eigenstates and eigenenergies of Hamiltonian (5) with a "(0)" superscript, we obtain

$$\langle\psi_m|\hat{\boldsymbol{H}}_{\vec{E}}|\psi_n\rangle \approx \langle\psi_m^{(0)}|\hat{\boldsymbol{H}}_{\vec{E}}|\psi_n^{(0)}\rangle - \sum_{k\neq m}\frac{\langle\psi_m^{(0)}|\hat{\boldsymbol{H}}_{Zee}|\psi_k^{(0)}|\rangle\langle|\psi_k^{(0)}|\hat{\boldsymbol{H}}_{\vec{E}}|\psi_n^{(0)}\rangle}{E_k^{(0)} - E_m^{(0)}} - \sum_{k\neq n}\frac{\langle\psi_m^{(0)}|\hat{\boldsymbol{H}}_{\vec{E}}|\psi_k^{(0)}|\rangle\langle|\psi_k^{(0)}|\hat{\boldsymbol{H}}_{Zee}|\psi_n^{(0)}\rangle}{E_k^{(0)} - E_n^{(0)}} \quad (8)$$

to leading order in $\boldsymbol{B}$. The sum over k includes other states in the ground quartet and higher excited states. The first term on the right-hand side represents the zero-field SEC, which would be exactly zero for Kramers systems in the absence of HFC. The second and third terms are the first-order contributions, and due to the small energy separations within the ground quartet entering the denominator, the zeroth-order contribution is vastly outweighed by the first-order contributions. We find that the SEC for NMR-like transitions is generally much smaller in zero-field than at 320 mT (Figs. S5–S7), which is due to the smaller effect that the electric field has on the HFC Hamiltonian than the crystal field Hamiltonian Supplementary Note 6.

The linear terms in the magnetic field in Eq. (8) can help explain some other trends in Fig. 3. For instance, we note that NMR-like couplings are generally smaller when the magnetic field is oriented along x, similarly to what we discussed above for EPR-like couplings, with the exception of the symmetry-preserving distortion E_y. This occurs for the same reason as

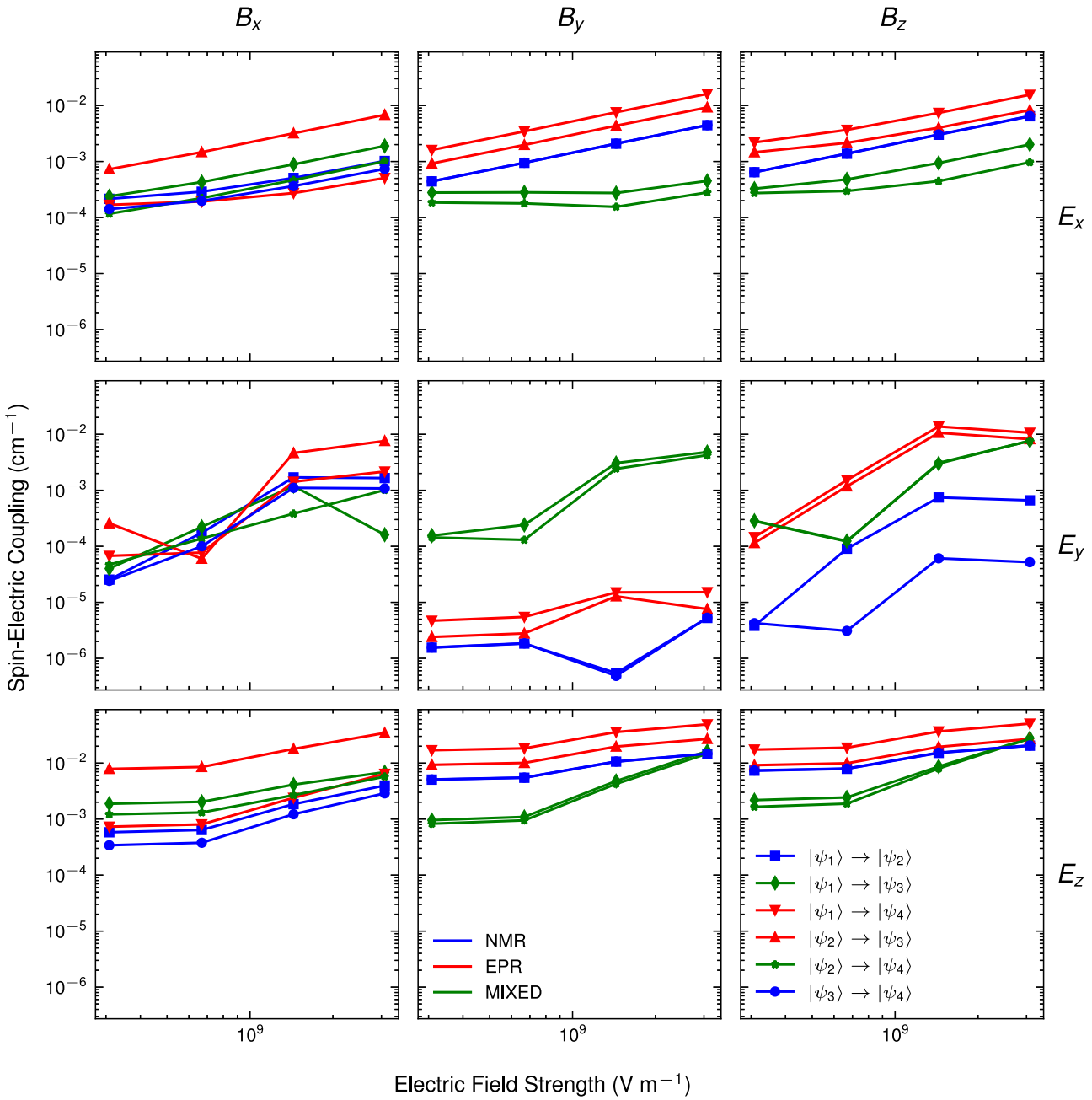

Fig. 3 | Spin-electric coupling anisotropy. The magnetic and electric field orientation dependence of the spin electric coupling as a function of electric field strength for each transition within the ground quartet of states. The colour of the line indicates the type of transition: NMR-like (blue), EPR-like (red), mixed (green), while the shape of the marker indicates the individual transition within the quartet. The spin-electric coupling was calculated using a magnetic field strength of 320 mT.

above: when the magnetic field is along x, the electronic Zeeman interaction does not cause significant mixing within the ground crystal field doublet, and the first-order correction in Eq. (8) vanishes (see Supplementary Note 1 for details).

Spin-electric coupling symmetry decomposition

In our previous work, we discussed the effect of symmetry-breaking or preserving distortions on the SEC[28]. Since we now consider both the electronic and nuclear degrees of freedom, we can identify if the symmetry of the distortion has a significant effect on the modulation of the HFC. We previously defined a symmetry-adapted coordinate basis $\boldsymbol{Z}$ in which atoms related by pseudo-symmetry are displaced in and out of phase and assigned to their irreducible representation of the C_2 point group[28]. We define the coupling $C_i^{(m,n)}(\hat{\boldsymbol{H}})$ (in cm^{-1}) below, which is the off-diagonal matrix element of a given Hamiltonian $\hat{\boldsymbol{H}}$ (i.e. $\hat{\boldsymbol{H}}_{\mathrm{HF}}$ or $\hat{\boldsymbol{H}}_{\mathrm{CF}}$) between states $|\psi_m\rangle$ and $|\psi_n\rangle$ that arises due to a displacement along the ith symmetry-adapted coordinate basis mode $\boldsymbol{Z}_i$.

$$C_i^{(m,n)}(\hat{\boldsymbol{H}}) = \left| \left(\hat{\boldsymbol{U}}_{\mathrm{eq}}^{\dagger} \frac{\partial \hat{\boldsymbol{H}}}{\partial Z_i} \hat{\boldsymbol{U}}_{\mathrm{eq}} \right)_{m,n} \right| \tag{9}$$

Where $\hat{\boldsymbol{U}}_{\mathrm{eq}}$ is the unitary operator that rotates the derivatives into the eigenstate basis of the equilibrium Hamiltonian. The coupling for each symmetry-adapted mode derivative is plotted and coloured according to its assignment to the A or B irreducible representation for both the modulation of the crystal field and the HFC (Fig. 4).

In general, modulations of the crystal field generate couplings that are approximately two orders of magnitude larger than the couplings arising from

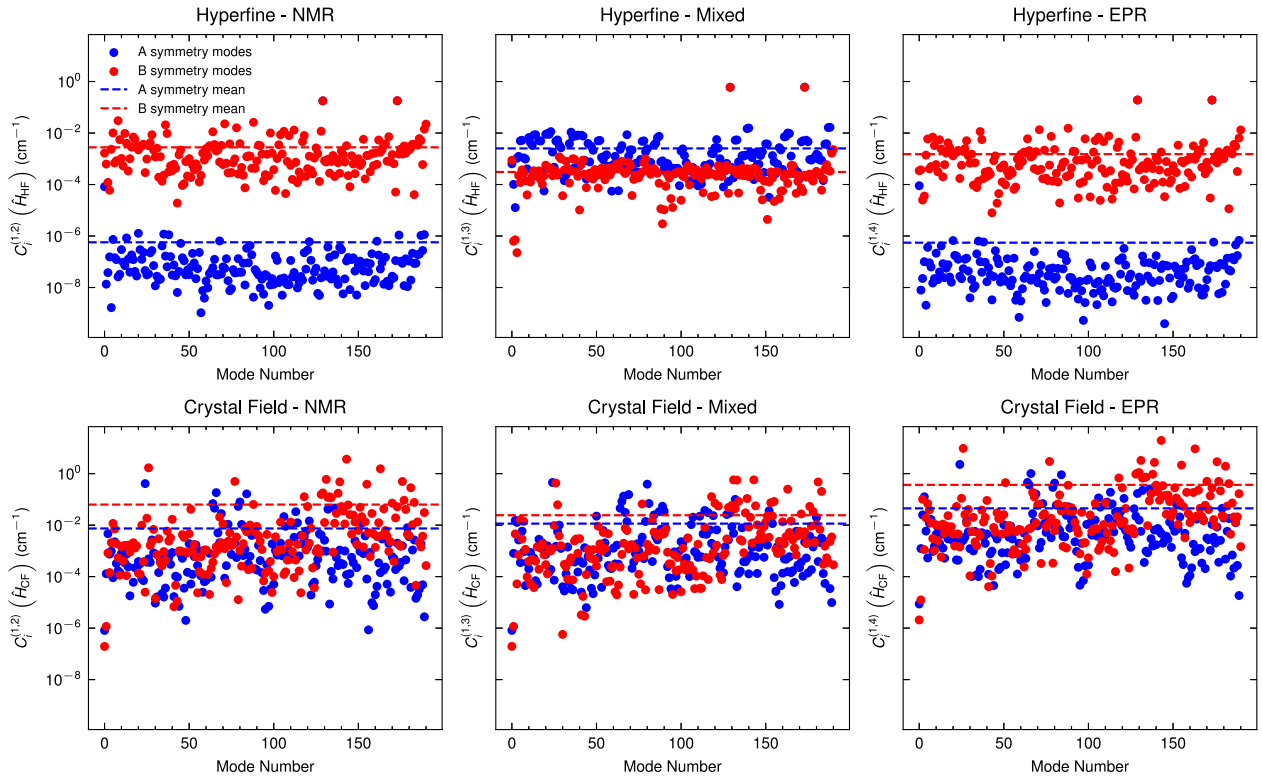

Fig. 4 | Spin electric coupling symmetry decomposition. The coupling generated in the crystal field and hyperfine coupling Hamiltonians due to a displacement along a symmetry adapted coordinate basis mode for each character of transition (NMR $|\psi_1\rangle \rightarrow |\psi_2\rangle$, EPR $|\psi_1\rangle \rightarrow |\psi_4\rangle$, mixed $|\psi_1\rangle \rightarrow |\psi_3\rangle$). Categorised by the symmetry of each modes distortion and projected into the eigenstate basis of the equilibrium Hamiltonian with a magnetic field of $B_y = 320$ mT.

modulation of the HFC for a given mode. However, the details of these differences are anisotropic. When the magnetic field is oriented along z or y (perpendicular to the N-Tm-N anisotropy axis) we observe a symmetry dependence of the HFC terms for the transitions with EPR and NMR character (Figs. 4 and S21). However, when the magnetic field is oriented along x (parallel to the anisotropy axis) the symmetry dependence vanishes (Fig. S20).

To elucidate this anisotropy, we can evaluate the hyperfine Hamiltonian derivatives when the Zeeman contribution is treated perturbatively (Supplementary Note 1 and Supplementary Note 9). For the off-diagonal matrix elements of the derivative of the hyperfine Hamiltonian with respect to the ith symmetry-adapted coordinate mode we have:

$$\langle\psi_m|\frac{\partial\hat{\boldsymbol{H}}_{\mathrm{HF}}}{\partial Z_i}|\psi_n\rangle \approx \langle\psi_m^{(0)}|\frac{\partial\hat{\boldsymbol{H}}_{\mathrm{HF}}}{\partial Z_i}|\psi_n^{(0)}\rangle - \sum_{k\neq m}\frac{\langle\psi_m^{(0)}|\hat{\boldsymbol{H}}_{\mathrm{Zee}}|\psi_k^{(0)}\rangle\langle\psi_k^{(0)}|\frac{\partial\hat{\boldsymbol{H}}_{\mathrm{HF}}}{\partial Z_i}|\psi_n^{(0)}\rangle}{E_k^{(0)}-E_m^{(0)}} - \sum_{k\neq n}\frac{\langle\psi_m^{(0)}|\frac{\partial\hat{\boldsymbol{H}}_{\mathrm{HF}}}{\partial Z_i}|\psi_k^{(0)}\rangle\langle\psi_k^{(0)}|\hat{\boldsymbol{H}}_{\mathrm{Zee}}|\psi_n^{(0)}\rangle}{E_k^{(0)}-E_n^{(0)}} \tag{10}$$

Analogously to the full electric field Hamiltonian treated in the same way (Eq. (8)), the derivatives of the hyperfine Hamiltonian depend on how the initial and final states are mixed with all other states due to Zeeman interaction. Hence, much like for our previous work considering only the electronic part,[28] the SEC arising from the HFC terms is small when magnetic fields are parallel to the magnetic anisotropy axis (i.e. the x-axis). Additionally, we also observe that the presence or absence of a symmetry effect is strongly dependent on the nature of the transition: for EPR and NMR transitions, the average coupling generated by B symmetry modes are at least one order of magnitude larger than the A symmetry modes for B_y and B_z (e.g. Fig. 4, top row, left and right panels), while for mixed character transitions the difference is much smaller (e.g. Fig. 4, top row, middle panel).

This behaviour arises because distortions of A symmetry have nearly zero contribution to mixing zero-field eigenstates of "forbidden" character. As previously discussed, the first-order terms have a much larger contribution that the zeroth-order term due to the small energy denominator. The first-order correction sums over all other states in the system ($k \neq m, n$), and therefore, for the mixed/ forbidden character transition, the matrix element which is near-zero for A symmetry is not included in the summation while this near-zero term is included in the summation for EPR/ NMR transitions (see Table S3). This is why we do not observe the symmetry effect for the mixed character transition, and we do for the EPR and NMR transitions.

Electric field spin dynamics

To demonstrate the potential for coherent state manipulation using electric fields under realistic experimental conditions, we now consider the spin dynamics of the ground quartet under the influence of resonant electric field pulses, in analogy to microwave field drives of pulsed EPR. The time-dependent spin Hamiltonian is constructed as $\hat{\boldsymbol{H}}(t) = \hat{\boldsymbol{H}}_{\mathrm{eq}} + \hat{\boldsymbol{H}}_{\vec{E}}\cos\omega_d t$, obtained simply by modulating the electric field Hamiltonian (6) at a frequency ω_d, which can be tuned to specific transitions. The time-evolution of the spin density matrix $\hat{\boldsymbol{\rho}}$ is determined by the master equation:

$$\frac{\partial\hat{\boldsymbol{\rho}}}{\partial t} = -\frac{i}{\hbar}\left[\hat{\boldsymbol{H}}(t),\hat{\boldsymbol{\rho}}\right] + \mathcal{D}_{\mathrm{el}}(\hat{\boldsymbol{\rho}}) + \mathcal{D}_{\mathrm{nuc}}(\hat{\boldsymbol{\rho}}) \tag{11}$$

To make sure that our timescales are relevant, we account for spin relaxation processes via the Lindblad superoperators[43] $\mathcal{D}_{\mathrm{el}}$ and $\mathcal{D}_{\mathrm{nuc}}$, which describe relaxation and dephasing acting on the electronic and nuclear spin, originating from spin-phonon coupling and dipolar interactions with nearby nuclei, respectively. If the energy separation between ground and first excited electronic Kramers doublets is sufficiently large compared to

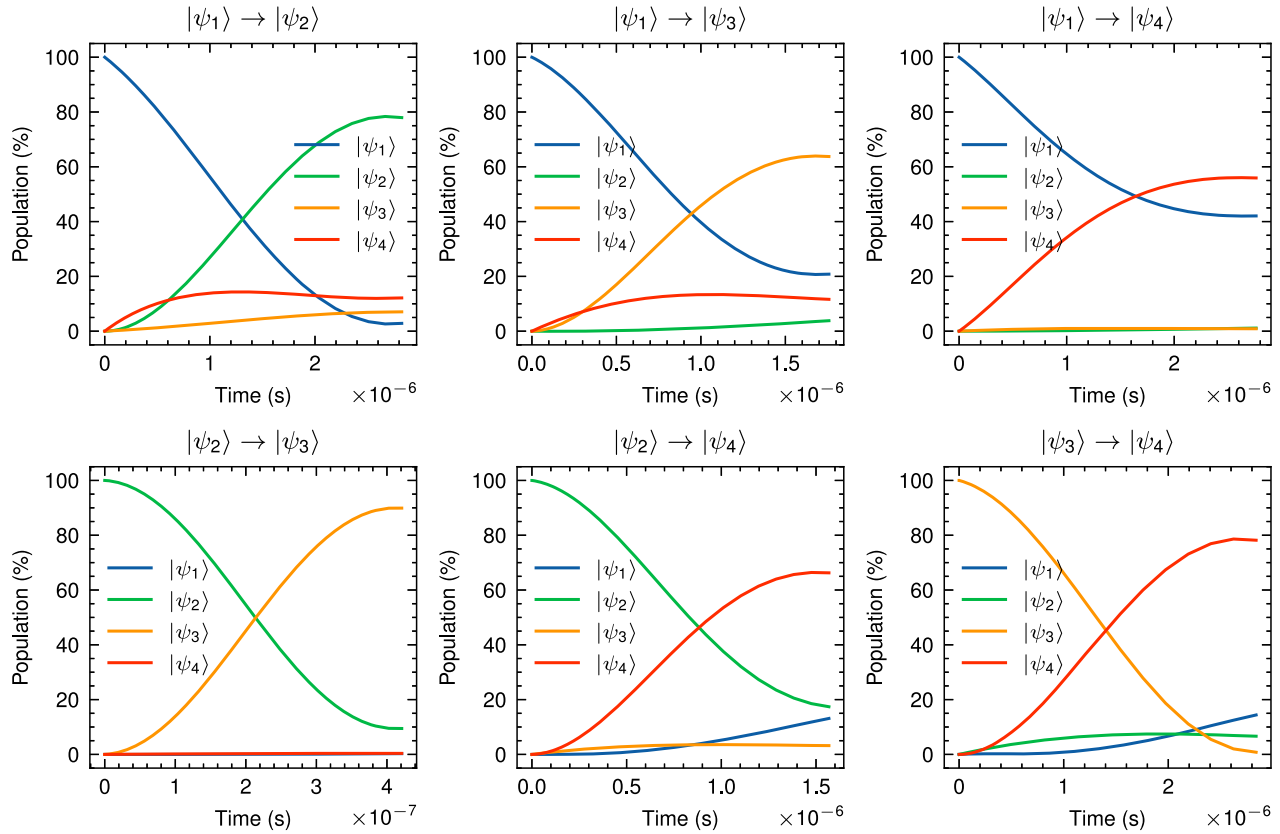

Fig. 5 | Electric field driven spin-dynamics. Spin-dynamics simulation of π-pulses for each transition in the ground quartet of $[Tm(N^{\dagger\dagger})_2]$, $B_x = 320$ mT, $E_z = 1 \times 10^6$ V m^{-1}. Using characteristic rates γ_{el} and γ_{nuc} for electronic and nuclear relaxation of 1μs^{-1} and 1ms^{-1} respectively.

thermal energy, the spin dynamics will be well-contained within the ground hyperfine quartet on timescales relevant to coherent spin manipulation. This condition is satisfied in $[Tm\{N(Si^iPr_3)_2\}_2]$ at cryogenic temperatures, where this energy separation is ca. 500 cm^{-1} or 700 K. Within the ground doublet, the effect of spin-phonon interactions is then described by the phenomenological dephasing superoperator

$$\mathcal{D}_{el}(\hat{\boldsymbol{\rho}}) = \sum_m \gamma_{el}\left(\hat{\boldsymbol{P}}_m\hat{\boldsymbol{\rho}}\hat{\boldsymbol{P}}_m - \frac{1}{2}\{\hat{\boldsymbol{P}}_m, \hat{\boldsymbol{\rho}}\}\right) \quad (12)$$

where m labels the two crystal field states in the ground Kramers doublet and $\hat{\boldsymbol{P}}_m$ is the projector $|m\rangle\langle m|$. We set the dephasing rate γ_{el} to 1μs^{-1}, corresponding to typical electron spin dephasing time for lanthanide molecules in solution[44].

We describe the effect of a nuclear spin bath on the Tm nuclear spin through the phenomenological superoperator

$$\mathcal{D}_{nuc}(\hat{\boldsymbol{\rho}}) = \sum_{ij=x,y,z} \gamma_{nuc}^{ij}\left(\hat{\boldsymbol{I}}_i\hat{\boldsymbol{\rho}}\hat{\boldsymbol{I}}_j - \frac{1}{2}\left\{\hat{\boldsymbol{I}}_j\hat{\boldsymbol{I}}_i, \hat{\boldsymbol{\rho}}\right\}\right), \quad (13)$$

which captures both longitudinal and transverse relaxation of the nuclear spin. The operators $\hat{\boldsymbol{I}}_i$ are components of the nuclear spin angular momentum operator $\hat{\boldsymbol{I}}$. We set all rates γ_{nuc}^{ij} to the same value $\gamma_{nuc} = 1$ms^{-1}, which is typical for bath-limited nuclear spin relaxation in the solid state[45].

From the energy levels at zero magnetic field (Fig. 2a), we can see that driving frequencies will be on the hundreds of MHz scale. We simulate the spin dynamics of the three distinct pulse types: NMR-like, EPR-like, and mixed/forbidden using a square electric field pulse. A square pulse is an idealised pulse in which the resonant electric field is turned on instantaneously, remains at a constant amplitude throughout the pulse, and is instantaneously turned off. Selective manipulation of individual transitions at zero magnetic field can be challenging, due to several transitions being spectrally close. In fact, when the driving frequency of the pulse is nearly resonant with multiple transitions, population transfer mainly occurs to the state that couples most strongly to the initial state via the electric field Hamiltonian $\hat{\boldsymbol{H}}_{\vec{E}}$.

We can improve selectivity by applying a magnetic field to enhance the energy separation of the states. Applying a magnetic field along x results in asymmetric energy splitting of the upper and lower doublet of states within the ground quartet (Fig. 2a); therefore, we set the magnetic field to 320 mT along B_x. This allows us to demonstrate coherent manipulation of each transition within the ground quartet via a resonant π-pulse, A 180° rotation within the Bloch sphere where all population is transferred from an initial state to a target state (Fig. 5), assuming an ideal initial condition where all spin population is concentrated in a single hyperfine state. We set the strength of the amplitude of the oscillating electric field to 10^6 V m^{-1}, which can be easily accessed in a realistic experiment[23,25,27,46].

Within our assumptions, the highest target population (90%) is obtained for the EPR-like transition $|\psi_2\rangle \rightarrow |\psi_3\rangle$, which also shows the fastest transition, needing a π-pulse duration of ~0.4 μs. In general, typical EPR π-pulses driven with transverse microwave radiation occur on the 10's ns time scale which is orders of magnitude faster than the predicted electric field pulse duration required. Among the transitions starting from the ground state, the largest target population (80%) is achieved for the NMR-like transition $|\psi_1\rangle \rightarrow |\psi_2\rangle$. Demonstrating, our aim to coherently modulate the nuclear degrees of freedom using an applied electric field. While driving can be achieved also for mixed transitions, these show a consistently lower population of the target state around 65%. However, we note that this can be further improved by using a larger electric field strength, thereby allowing shorter pulses which reduce the effect of dephasing and nuclear spin relaxation, at the expense of larger frequency bandwidth. Other control schemes based on more complex pulse sequences may also be a viable option, such as dynamical decoupling[47,48].

We stress that, in order to access not only EPR-like but also NMR-like and mixed/forbidden transitions experimentally, it is imperative to consider not only the magnitude of the applied oscillating electric field but also the magnitude of the static magnetic field. This static magnetic field determines the energy splitting of the ground quartet states and, consequently, the driving frequency of each transition. But furthermore, the choice of magnetic field also influences dephasing. This is because the equilibrium eigenstates are not separable at small magnetic fields, and hence the dephasing operators in Eq. (12) mix states within the ground quartet, causing unwanted population transfer between crystal field eigenstates. However, at larger magnetic fields, where the equilibrium eigenstates are separable, the unwanted population transfer is suppressed (Supplementary Fig. S23). For more details on the separability of the equilibrium eigenstate as a function of magnetic field, refer to Supplementary Note 2.

Conclusion

We have investigated the influence of the nuclear spin on the SEC in $[Tm\{N(Si^iPr_3)_2\}_2]$ with ab initio simulations. We have found that the molecular distortion in an electric field can modulate the HFC, thus enabling electric field control of the nuclear spin. However, the SEC for transitions with mainly NMR character is smaller than those with EPR character due to the smaller geometric dependence of the hyperfine tensor compared to the crystal field parameters. None-the-less, the dependence of the SEC on the symmetry-breaking/preserving nature of the structural distortion is observed in both cases. Despite the HFC enabling SEC at zeroth-order, this effect is small compared to the coupling that arises in the presence of a magnetic field. Time-dependent simulations of nuclear and electron spin dynamics, accounting for decoherence and dephasing, show that application of a magnetic field enhances the ability for coherent manipulation of selective transitions. This is partly due to a decoupling of the electronic and nuclear degrees of freedom in a magnetic field, but also by separating the different resonant frequencies. This work highlights the interplay between electronic and nuclear spins under the influence of electric field control, which will inform the development of electro-nuclear spin qudits for quantum information processing and quantum transduction.

Data availability

Research data is available at FigShare via https://doi.org/10.48420/30689570.

Code availability

Code is as described in Morrillo et. al., *J. Am. Chem. Soc.*, **2024** 146 (37), 25841-25851.

Received: 15 August 2025; Accepted: 27 November 2025;
Published online: 18 December 2025

References

1. Wasielewski, M. R. et al. Exploiting chemistry and molecular systems for quantum information science. *Nat. Rev. Chem.* **4**, 490–504 (2020).
2. Moreno-Pineda, E., Godfrin, C., Balestro, F., Wernsdorfer, W. & Ruben, M. Molecular spin qudits for quantum algorithms. *Chem. Soc. Rev.* **47**, 501–513 (2018).
3. Moreno-Pineda, E. et al. Observation of cooperative electronic quantum tunneling: increasing accessible nuclear states in a molecular qudit. *Inorg. Chem.* **57**, 9873–9879 (2018).
4. Wernsdorfer, W. & Ruben, M. Synthetic hilbert space engineering of molecular qudits: isotopologue chemistry. *Adv. Mater.* **31**, 1806687 (2019).
5. Godfrin, C. et al. Operating quantum states in single magnetic molecules: implementation of grover's quantum algorithm. *Phys. Rev. Lett.* **119**, 187702 (2017).
6. Chicco, S. et al. Proof-of-concept quantum simulator based on molecular spin qudits. *J. Am. Chem. Soc.* **146**, 1053–1061 (2024).
7. Latham, E., Bowen, A. M., Cox, N. & Chilton, N. F. Inverse design of molecular qudits for quantum circuitry. *Inorg. Chem.* https://doi.org/10.1021/acs.inorgchem.5c00298 (2025).
8. Mezzadri, M., Lepori, L., Chiesa, A. & Carretta, S. Dephasing-tolerant quantum sensing for transverse magnetic fields with spin qudits. *Quantum Sci. Technol.* **10**, 015045 (2024).
9. Chizzini, M. et al. Molecular nanomagnets with competing interactions as optimal units for qudit-based quantum computation. *Phys. Rev. Res.* **4**, 043135 (2022).
10. Chiesa, A., Petiziol, F., Chizzini, M., Santini, P. & Carretta, S. Theoretical design of optimal molecular qudits for quantum error correction. *J. Phys. Chem. Lett.* **13**, 6468–6474 (2022).
11. Luis, F. et al. A dissymmetric [gd2] coordination molecular dimer hosting six addressable spin qubits. *Commun. Chem.* **3**, 176 (2020).
12. Castro, A., García Carrizo, A., Roca, S., Zueco, D. & Luis, F. Optimal control of molecular spin qudits. *Phys. Rev. Appl.* **17**, 064028 (2022).
13. Gimeno, I. et al. Broad-band spectroscopy of a vanadyl porphyrin: a model electronuclear spin qudit. *Chem. Sci.* **12**, 5621–5630 (2021).
14. Miao, K. C. et al. Universal coherence protection in a solid-state spin qubit. *Science* **369**, 1493–1497 (2020).
15. Gaita-Ariño, A., Luis, F., Hill, S. & Coronado, E. Molecular spins for quantum computation. *Nat. Chem.* **11**, 301–309 (2019).
16. Roca-Jerat, S., Macaluso, E., Chiesa, A., Santini, P. & Carretta, S. Simulating open quantum systems with molecular spin qudits. *Mater. Horiz.***12**, 3918–3928 (2025).
17. Mezzadri, M., Chiesa, A., Lepori, L. & Carretta, S. Fault-tolerant computing with single-qudit encoding in a molecular spin. *Mater. Horiz.* **11**, 4961–4969 (2024).
18. Lim, S., Liu, J. & Ardavan, A. Fault-tolerant qubit encoding using a spin-7/2 qudit. *Phys. Rev. A* **108**, 062403 (2023).
19. Lim, S., Vaganov, M. V., Liu, J. & Ardavan, A. Demonstrating experimentally the encoding and dynamics of an error-correctable logical qubit on a hyperfine-coupled nuclear spin qudit. *Phys. Rev. Lett.* **134**, 070603 (2025).
20. DiVincenzo, D. P. The physical implementation of quantum computation. *Fortschr. Phys. Prog. Phys.* **48**, 771–783 (2000).
21. Samach, G. O. et al. Lindblad tomography of a superconducting quantum processor. *Phys. Rev. Appl.* **18**, 064056 (2022).
22. van Slageren, J. Spin–electric coupling. *Nat. Mater.* **18**, 300–301 (2019).
23. Robert, J., Parizel, N., Turek, P. & Boudalis, A. K. Polyanisotropic magnetoelectric coupling in an electrically controlled molecular spin qubit. *J. Am. Chem. Soc.* **141**, 19765–19775 (2019).
24. Shiddiq, M. et al. Enhancing coherence in molecular spin qubits via atomic clock transitions. *Nature* **531**, 348–351 (2016).
25. Liu, J. et al. Quantum coherent spin-electric control in a molecular nanomagnet at clock transitions. *Nat. Phys.* **17**, 1205–1209 (2021).
26. Vaganov, M. V. et al. Chemical tuning of quantum spin-electric coupling in molecular nanomagnets. *Nat. Chem.* **17**, 1903–1909 (2025).
27. Liu, J. et al. Electric field control of spins in molecular magnets. *Phys. Rev. Lett.* **122**, 037202 (2019).
28. Morrillo, W. T., Cumming, H. I. J., Mattioni, A., Staab, J. K. & Chilton, N. F. Ab initio design of molecular qubits with electric field control. *J. Am. Chem. Soc.* **146**, 25841–25851 (2024).
29. Scaramucci, A., Bousquet, E., Fechner, M., Mostovoy, M. & Spaldin, N. A. Linear magnetoelectric effect by orbital magnetism. *Phys. Rev. Lett.* **109**, 197203 (2012).
30. Aquilante, F. et al. Modern quantum chemistry with [open]molcas. *J. Chem. Phys.* **152**, 214117 (2020).
31. Fdez. Galván, I. et al. OpenMolcas: from source code to insight. *J. Chem. Theory Comput.* **15**, 5925–5964 (2019).
32. Li Manni, G. et al. The OpenMolcas web: a community-driven approach to advancing computational chemistry. *J. Chem. Theory Comput.* **19**, 6933–6991 (2023).

33. Malmqvist, P. K. & Roos, B. O. The CASSCF state interaction method. *Chem. Phys. Lett.* **155**, 189–194 (1989).
34. Malmqvist, P. K., Roos, B. O. & Schimmelpfennig, B. The restricted active space (RAS) state interaction approach with spin-orbit coupling. *Chem. Phys. Lett.* **357**, 230–240 (2002).
35. Peng, D. & Reiher, M. Exact decoupling of the relativistic Fock operator. *Theor. Chem. Acc.* **131**, 1081 (2012).
36. Peng, D. & Reiher, M. Local relativistic exact decoupling. *J. Chem. Phys.* **136**, 244108 (2012).
37. Aquilante, F., Lindh, R. & Bondo Pedersen, T. Unbiased auxiliary basis sets for accurate two-electron integral approximations. *J. Chem. Phys.* **127**, 114107 (2007).
38. Birnoschi, L. & Chilton, N. F. Hyperion: A new computational tool for relativistic ab initio hyperfine coupling. *J. Chem. Theory Comput.* **18**, 4719–4732 (2022).
39. angmom-suite. https://pypi.org/project/angmom-suite/.
40. Stoll, S. & Schweiger, A. EasySpin, a comprehensive software package for spectral simulation and analysis in EPR. *J. Magn. Reson.* **178**, 42–55 (2006).
41. Goodwin, C. A. et al. Physicochemical properties of near-linear lanthanide(II) bis(silylamide) complexes (Ln = Sm, Eu, Tm, Yb). *Inorg. Chem.* **55**, 10057–10067 (2016).
42. Chilton, N. F., Anderson, R. P., Turner, L. D., Soncini, A. & Murray, K. S. Phi: A powerful new program for the analysis of anisotropic monomeric and exchange-coupled polynuclear d- and f-block complexes. *J. Comput. Chem.* **34**, 1164–1175 (2013).
43. Breuer, H. & Petruccione, F. *The Theory of Open Quantum Systems* https://books.google.co.uk/books?id=0Yx5VzaMYm8C (Oxford University Press, 2002).
44. Pedersen, K. S. et al. Toward molecular 4f single-ion magnet qubits. *J. Am. Chem. Soc.* **138**, 5801–5804 (2016).
45. Onizhuk, M. & Galli, G. Bath-limited dynamics of nuclear spins in solid-state spin platforms. *Phys. Rev. B* **108**, 075306 (2023).
46. Le Mardelé, F. et al. Probing spin-electric transitions in a molecular exchange qubit. *Nat. Commun.* **16**, 1198 (2025).
47. Viola, L. & Lloyd, S. Dynamical suppression of decoherence in two-state quantum systems. *Phys. Rev. A* **58**, 2733–2744 (1998).
48. Sutherland, R. T. & Erickson, S. D. Passive dynamical decoupling of trapped-ion qubits and qudits. *Phys. Rev. A* **109**, 022620 (2024).

Acknowledgements

The authors would like to acknowledge the assistance given by Research IT and the use of the Computational Shared Facility at The University of Manchester. The authors would like to thank The Royal Society (URF191320), the European Research Council (ERC-2019-STG-851504, CoG-816268) and The University of Manchester for funding. We acknowledge the EPSRC UK National Electron Paramagnetic Resonance Service (EP/S033181/1). We thank Mr Adam Brookfield for technical support, Dr Jack Emerson-King for sample sealing, and Prof. Stephen Hill for insightful conversations.

Author contributions

W.T.M., N.F.C., and A.M. conceived the concept. W.T.M. performed the ab initio calculations, calculations of the SEC, spin dynamics simulations, and symmetry decomposition. A.M. performed characterisation of transitions and calculations of the entropy of entanglement. N.F.C. supervised the project. W.J.A.B. collected and interpreted the experimental EPR spectrum. D.P.M. supervised the synthesis of the sample.

Competing interests

The authors declare no competing interests.

Additional information

Supplementary information The online version contains supplementary material available at https://doi.org/10.1038/s42004-025-01852-0.

Correspondence and requests for materials should be addressed to Nicholas F. Chilton.

Peer review information *Communications Chemistry* thanks the anonymous reviewers for their contribution to the peer review of this work.